# Robust wrinkled $MoS_2$/N-C bifunctional electrocatalysts interfaced with single Fe atoms for wearable zinc-air batteries

Yan Yan[a,b], Shuang Liang[a], Xiang Wang[c], Mingyue Zhang[a], Shu-Meng Hao[a], Xun Cui[a], Zhiwei Li[d], and Zhiqun Lin[a,1]

[a]School of Materials Science and Engineering, Georgia Institute of Technology, Atlanta, GA 30332; [b]School of Chemistry and Materials Science, Jiangsu Key Laboratory of Green Synthetic Chemistry for Functional Materials, Jiangsu Normal University, Xuzhou 221116, China; [c]Chemical Sciences Division, Oak Ridge National Laboratory, Oak Ridge, TN 37831; and [d]Shenzhen Cloud Computing Center, National Supercomputing Center, Shenzhen 518055, China

Edited by Alexis T. Bell, University of California, Berkeley, CA, and approved August 30, 2021 (received for review June 9, 2021)

**The ability to create highly efficient and stable bifunctional electrocatalysts, capable of oxygen reduction reaction (ORR) and oxygen evolution reaction (OER) in the same electrolyte, represents an important endeavor toward high-performance zinc-air batteries (ZABs). Herein, we report a facile strategy for crafting wrinkled $MoS_2$/*N*-doped carbon core/shell nanospheres interfaced with single Fe atoms (denoted $MoS_2$@Fe-*N*-C) as superior ORR/OER bifunctional electrocatalysts for robust wearable ZABs with a high capacity and outstanding cycling stability. Specifically, the highly crumpled $MoS_2$ nanosphere core is wrapped with a layer of single-Fe-atom-impregnated, *N*-doped carbon shell (i.e., Fe-*N*-C shell with well-dispersed $FeN_4$ sites). Intriguingly, $MoS_2$@Fe-*N*-C nanospheres manifest an ORR half-wave potential of 0.84 V and an OER overpotential of 360 mV at 10 mA·cm$^{-2}$. More importantly, density functional theory calculations reveal the lowered energy barriers for both ORR and OER, accounting for marked enhanced catalytic performance of $MoS_2$@Fe-*N*-C nanospheres. Remarkably, wearable ZABs assembled by capitalizing on $MoS_2$@Fe-*N*-C nanospheres as an air electrode with an ultralow area loading (i.e., 0.25 mg·cm$^{-2}$) display excellent stability against deformation, high special capacity (i.e., 442 mAh·g$^{-1}{}_{Zn}$), excellent power density (i.e., 78 mW·cm$^{-2}$) and attractive cycling stability (e.g., 50 cycles at current density of 5 mA·cm$^{-2}$). This study provides a platform to rationally design single-atom-interfaced core/shell bifunctional electrocatalysts for efficient metal-air batteries.**

single Fe atoms | $MoS_2$ nanospheres | bifunctional electrocatalysts | ORR/OER | zinc-air batteries

Metal-air batteries represent a class of promising energy storage devices composed of a metal negative electrode electrochemically coupled to an air-breathing positive electrode through a suitable electrolyte (1). Among them, aqueous zinc-air batteries (ZABs) are widely recognized as one of the most promising devices due to their high theoretical energy density (1,086 Wh·kg$^{-1}$), low cost (<\$10 kW$^{-1}$·h$^{-1}$) and inherent safety (2). Despite these advantageous attributes, the commercialization of rechargeable ZABs is plagued by their limited energy density and poor cycle life due to the inefficiency of air catalysts. In rechargeable ZABs, the oxygen reduction reaction (ORR) and oxygen evolution reactions (OER) take place at the air electrode in discharging and charging processes, respectively. Thus, the overall energy efficiency of ZABs is dictated by ORR/OER at the air electrode, which involves multiple proton-coupled electron transfers that are sluggish in nature, thereby resulting in small current density and large electrode polarization of ZABs (3). Despite the prominent electrocatalytic activity of Pt-based metals and Ir- and Ru-based metals toward ORR and OER, respectively, the scarce abundance, high cost, poor physical stability, and insufficient bifunctionaility hinder their large-scale use in sustainable energy devices (4). Clearly, the ability to develop inexpensive bifunctional electrocatalysts with high kinetics and long durability is the key to their utility for constructing efficient and stable ZABs.

Two-dimensional transition-metal dichalcogenides (e.g., $MoS_2$, $WS_2$, and $MoSe_2$) have garnered much attention in the context of catalysis due to their reduced dimensionality and a set of intriguing chemical properties (e.g., high catalytic activity, outstanding chemical stability, etc.) (5, 6). Particularly, $MoS_2$ has been extensively studied as a unique electrocatalyst for hydrogen evolution reaction (HER) (7). It is notable that S-vacancies and sulfur-terminated edges of $MoS_2$ flakes not only activate HER but also accelerate OER (8, 9). Intriguingly, by creating $MoS_2$-containing heterojunctions (e.g., $MoS_2/WS_2$, $MoS_2/Ni_3S_2$, etc.) (10–12), the resulting composites manifest the enhanced OER activity over the pristine $MoS_2$. Nonetheless, due to direct exposure to alkaline electrolytes, $MoS_2$-based composites may be severely oxidized during the OER process, leading to the rapid decay in the activity (13). In addition, regardless of high OER activity, these composites still suffer from sluggish ORR kinetics, thereby limiting their use in ZABs. In sharp contrast, nitrogen-coordinated transition-metal atoms–anchored carbon nanomaterials (denoted M–N–C), in particular Fe–N–C, have emerged as a class of appealing ORR electrocatalysts owing to their earth abundance, tunable surface chemistry, modified electronic structure, and optimal oxygen absorption (14). Generally, downsizing active species of Fe–N–C catalysts to the single-atom scale could promote maximum atom-utilization efficiency via fully exposing the active sites, thereby greatly enhancing the intrinsic nature of

## Significance

Single-atom catalysis involves precise modulation of structures at the atomic level to markedly enhance catalytic activity. This work explores wrinkled $MoS_2$@Fe-*N*-C core/shell nanospheres with atomic Fe-doped surface and interface ($MoS_2$/Fe-*N*-C) as highly efficient bifunctional catalysts for both oxygen reduction and evolution reactions (ORR and OER), rivaling the ORR and OER activity of Pt/C and Ir/C, respectively. The robust performance can be attributed to the unique $MoS_2$/Fe-*N*-C interface, at which the highly active Fe-$N_4$ moieties coupled with the grain boundary of $MoS_2$ simultaneously reduce the energy barriers of ORR and OER. Notably, the Fe-N-C shell protects the $MoS_2$ core from corrosion during the ORR and OER processes in the alkaline electrolyte, leading to a long-term stability for the as-constructed zinc-air batteries.

Author contributions: Y.Y. and Z. Lin designed research; Y.Y., S.L., X.W., M.Z., S.-M.H., X.C., and Z. Li performed research; Y.Y. and Z. Lin analyzed data; and Y.Y. and Z. Lin wrote the paper.

The authors declare no competing interest.

This article is a PNAS Direct Submission.

[1]To whom correspondence may be addressed. Email: zhiqun.lin@mse.gatech.edu.

This article contains supporting information online at https://www.pnas.org/lookup/suppl/doi:10.1073/pnas.2110036118/-/DCSupplemental.

catalysts (15, 16). Furthermore, the nitrogen-doped carbon matrix could not only firmly stabilize the highly energetic single atoms through the metal-nitrogen interaction to mitigate the aggregation of metal atoms but also effectively facilitate the transport of ORR-relevant species (i.e., O*, OH*, OOH*, and $O_2$*) during the electrocatalytic process (17, 18). In this context, the capability of creating $MoS_2$/Fe-*N*-C heterostructures composed of atomic Fe catalysts positioned at the interface may enable the construction of electrocatalysts with enhanced bifunctional ORR/OER activities. This, however, has yet to be largely explored.

Herein, we report a general and robust route to crafting highly crumpled nanospheres composed of a $MoS_2$ core blanketed by a single-metal-atom-coordinated, *N*-doped carbon shell (i.e., $MoS_2$@M-*N*-C; M = Fe, Co, Ni) that function as stable ORR/OER bifunctional electrocatalysts for wearable, high-capacity, and outstanding-cycling-stability ZABs. Taking $MoS_2$@Fe-*N*-C as an example, one Fe single atom coordinates with four N atoms into a Fe-$N_4$ site at the $MoS_2$/Fe-*N*-C interface, as corroborated by X-ray absorption fine structure study. The Fe-$N_4$ sites are supported by carbon matrix as Fe-*N*-C shell, which drapes on the surface of $MoS_2$ nanospheres, forming $MoS_2$@Fe-*N*-C nanospheres that possess ample $MoS_2$/Fe-*N*-C interface. Notably, the spherical structure of $MoS_2$@Fe-*N*-C nanospheres could greatly prevent the aggregation of active sites, exhibiting sufficient electrochemical stability. Moreover, density functional theory (DFT) calculations signify that $MoS_2$/Fe-*N*-C interface could lower the reaction barriers of ORR and OER. Consequently, $MoS_2$@Fe-*N*-C nanospheres deliver superior bifunctional catalytic activity with a reversible oxygen overpotential of 0.86 V and long-term durability in the alkaline solution. More importantly, the Fe-*N*-C

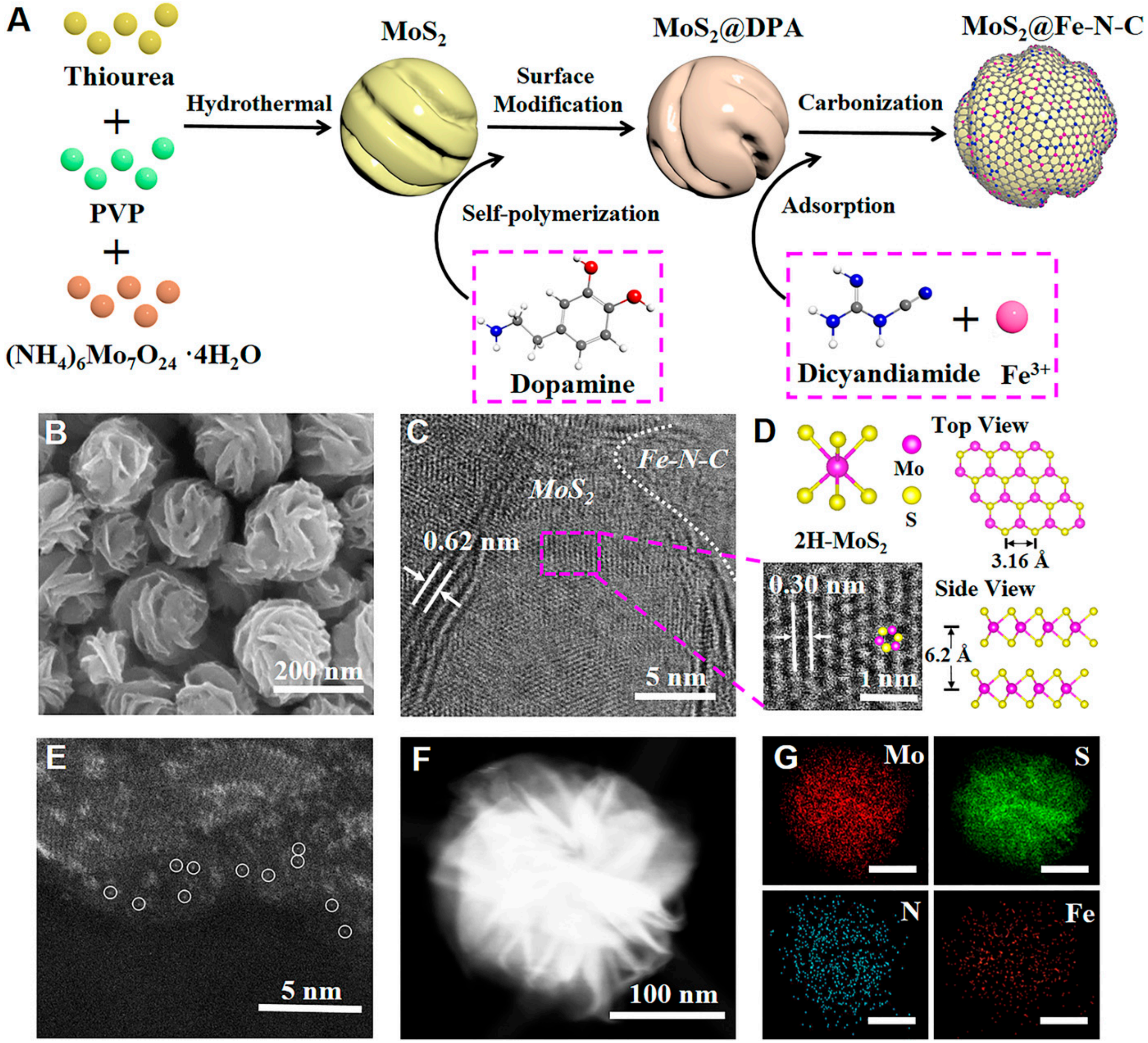

**Fig. 1.** (*A*) Schematic illustration of synthesis route to $MoS_2$@Fe-*N*-C NS, where the C, H, O, N, and S atoms are color-coded in gray, white, red, blue, and yellow, respectively. (*B*) SEM image and (*C*) HRTEM image of $MoS_2$@Fe-*N*-C NSs. (*D*) HRTEM image (*Lower left*), corresponding to the purple dashed area in *C*, structural model of 2H-$MoS_2$ (*Upper left*), and top view (*Upper right*) and side view (*Lower right*) of $MoS_2$ sheets, respectively. (*E*) AC HAADF-STEM image of $MoS_2$@Fe-*N*-C NS. (*F*) HAADF-STEM image, and (*G*) element maps (Mo: red, S: green, N: blue, Fe: orange; scale bar = 100 nm) of $MoS_2$@Fe-*N*-C NS.

shell not only accelerates the electrocatalytic activity of $MoS_2$ nanospheres but also minimizes the corrosion in alkaline electrolyte. Finally, $MoS_2$@Fe-*N*-C nanospheres are employed as an air cathode in a flexible zinc-air battery, displaying a high power density of 78 $mW\cdot cm^{-2}$, an excellent special capacity of 442 $mAh\cdot g^{-1}{}_{Zn}$, and an outstanding stability with an ultralow area loading of 0.25 $mg\cdot cm^{-2}$. As such, creating $MoS_2$@*N*-doped carbon nanospheres containing metal single atoms constrained at the $MoS_2$/*N*-doped carbon interface represents a facile strategy for constructing active and durable ORR/OER bifunctional electrocatalysts and in turn high-performance air electrodes for ZABs.

## Results and Discussion

**Crafting of $MoS_2$@Fe-*N*-C Nanospheres.** Fig. 1*A* depicts the crafting of $MoS_2$@Fe-*N*-C nanospheres (NSs) composed of $MoS_2$ NS as the core and single-Fe-atoms-anchored *N*-doped carbon matrix as the shell. Specifically, $MoS_2$ NSs were produced via one-step hydrothermal reaction of ammonium molybdate tetrahydrate, thiourea and poly(vinylpyrrolidone) (PVP) (*SI Appendix*, Experimental Section). As shown in *SI Appendix*, Fig. S1*A*, as-prepared $MoS_2$ NSs with a winkled surface are highly uniform, having an average diameter of ~200 nm. Notably, transmission electron microscopy (TEM) reveals that few-layer $MoS_2$ nanosheets are radially oriented to the NS with a interplanar spacing of 0.62 nm, which is consistent with the expanded *d* spacing of the (002) planes of hexagonal $MoS_2$ (*SI Appendix*, Fig. S2). Subsequently, dopamine-modified $MoS_2$ NSs (denoted $MoS_2$@DPA) was yielded via self-polymerization of dopamine monomers in the presence of $MoS_2$ NSs (Fig. 1*A*). Meanwhile, the dicyandiamide (DICY) molecules, containing two amine and two cyanogen groups, can strongly coordinate with the $Fe^{3+}$ ions, forming a DICY-Fe coordination compound (*SI Appendix*, Fig. S3). Notably, DICY-Fe can be readily adsorbed on the surface of the modified $MoS_2$@DPA NSs through hydrogen bonds between DICY-Fe and polydopamine (i.e., via amine-hydroxyl as well as amine-pyrrolyl hydrogen bonds). Finally, after pyrolysis under a nitrogen atmosphere at 800 °C, the coated DICY-Fe-PDA layers on $MoS_2$ NSs were carbonized into *N*-doped carbon, and the coordinated $Fe^{3+}$ ions were transformed into highly dispersed Fe single atoms, resulting in core/shell NSs comprising the $MoS_2$ core coated by a single-Fe-atom-coordinated, *N*-doped carbon shell (i.e., $MoS_2$@Fe-*N*-C NSs; Fig. 1*A*).

The resulting $MoS_2$@Fe-*N*-C NSs exhibit the spherical structure with a winkled surface, retaining the original morphology and size of the $MoS_2$ NSs, as revealed by the scanning electron microscopy (SEM) image (Fig. 1*B*) and TEM images (*SI Appendix*, Fig. S4). A high-resolution TEM (HRTEM) image of $MoS_2$@Fe-*N*-C NSs clearly shows the interlayer distance of 0.62 and 0.30 nm (Fig. 1 *C* and *D*), which can be indexed to the (002) and (100) facets, respectively, of hexagonal $MoS_2$ (2H-$MoS_2$) according to the respective Joint Committee on Power Diffraction Standards (JCPDS) card number of 37-1492 (*SI Appendix*, Fig. S2). Interestingly, graphitic carbon structures are also clearly evident at the edge of the $MoS_2$ nanosheets (Fig. 1*C*), confirming the formation of Fe-*N*-C shell. More importantly, no visible nanoparticles or clusters can be seen from the TEM images, and no obvious signals for metallic Fe species were detected in the powder X-ray diffraction (PXRD) pattern of $MoS_2$@Fe-*N*-C NSs (*SI Appendix*, Fig. S2), implying that Fe atoms may exist in an atomically dispersed form. Furthermore, atomic dispersion of Fe was substantiated by aberration-corrected high-angle annular dark-field scanning TEM (AC HAADF-STEM) analysis (Fig. 1*E*), displaying some individual bright dots (marked with white circles), corresponding to isolated single Fe atoms. Moreover, the element mapping images (Fig. 1 *F* and *G*) show the uniform distribution of Fe and N over the $MoS_2$/Fe-*N*-C interface and Fe-*N*-C shell. Inductively coupled plasma atomic emission spectroscopy (ICP-AES) analysis indicates that the weight fraction of Fe in the formed $MoS_2$@Fe-*N*-C NSs is 1.02 wt%.

In addition, $MoS_2$@Co-*N*-C NSs, $MoS_2$@Ni-*N*-C NSs, and $MoS_2$ NSs were also crafted for comparison. The $MoS_2$@Co-*N*-C NSs and $MoS_2$@Ni-*N*-C NSs were prepared by the same synthesis approach as $MoS_2$@Fe-*N*-C NSs (*SI Appendix*, Experimental Section). In addition, the representative characterization results of $MoS_2$@Co-*N*-C NSs and $MoS_2$@Ni-*N*-C NSs are discussed in *SI Appendix*, Figs. S5 and S6, respectively.

**Characterization of $MoS_2$@Fe-*N*-C Nanospheres.** To investigate the surface composition and electronic structure of $MoS_2$@Fe-*N*-C NSs, X-ray photoelectron spectroscopic (XPS) measurements were performed. The typical XPS survey spectrum (*SI Appendix*, Fig. S7) shows the coexistence of Mo (21.5 at%), S (40.3 at%), Fe (1.1 at%), N (10.2 at%), and C (20.9 at%) in $MoS_2$@Fe-*N*-C NSs. For $MoS_2$ NSs, Mo possesses two main subpeaks of Mo $3d_{3/2}$ and Mo $3d_{5/2}$ at 232.5 and 229.3 eV, respectively. However, the binding energy of Mo $3d_{3/2}$ and Mo $3d_{5/2}$ in $MoS_2$@Fe-*N*-C NSs shift to 232.6 and 229.4 eV, respectively (Fig. 2*A*). In addition, two minor subpeaks for $Mo^{6+}$ $3d_{3/2}$ and $Mo^{6+}$ $3d_{5/2}$ appear at 235.8 eV and 323.8 eV, respectively, suggesting the oxidation of a small amount of $MoS_2$ NSs during the carbonization process (19). Similarly, S $2p_{3/2}$ and S $2p_{1/2}$ signal in the case of $MoS_2$@Fe-*N*-C NSs also exhibit a positive shift of ~0.1 eV relative to that in $MoS_2$ NS (*SI Appendix*, Fig. S8*A*). These results substantiate the presence of electronic interaction between $MoS_2$ and Fe-*N*-C, signifying the formation of the coupled $MoS_2$/Fe-*N*-C interface (20, 21). The high-resolution C 1s spectrum exhibits three peaks at 287.4, 285.7, and 284.6 eV, which can be assigned to C-O, C-N, and C-C/C = C groups, respectively (*SI Appendix*, Fig. S8*B*). Carbon-oxygen species are regarded as defects which facilitate the ORR in the alkaline media (17, 22). The high-resolution Fe 2p spectrum shows two pairs of peaks for $Fe^{2+}$ (709.8 and 722.8 eV) and $Fe^{3+}$ (713.3 and 725.6 eV) (*SI Appendix*, Fig. S8*C*). Additionally, the peak around 720.3 eV can be ascribed to $Fe–N_x$ species, confirming the formation of $Fe–N_4$ configuration (23). The high-resolution N 1s spectrum could be well deconvoluted into three peaks located at 400.9, 399.3 and 398.2 eV, which are assigned to graphitic N, pyrrolic N, and pyridinic N, respectively (24) (*SI Appendix*, Fig. S8*D*). It has been widely recognized that the pyridinic N plays a vital role in forming $Fe–N_x$ active sites with a modified local electronic structure, and the graphitic N species facilitate the occurrence of a 4-electron transfer pathway during the ORR (25). Therefore, the high content of both pyridinic N and graphitic N in $MoS_2$@Fe-*N*-C NSs not only provides ample sites to anchor single Fe atoms but also imparts the enhanced ORR activity.

**Structures of Single Fe Atom Sites.** To scrutinize the chemical state and coordination environment of Fe-*N*-C shell in $MoS_2$@Fe-*N*-C NSs at atomic level, X-ray absorption fine structure (XAFS) measurements were performed, and commercial Fe foil and $Fe_2O_3$ were employed as benchmarks. As shown in Fig. 2*B*, the absorption edge of X-ray absorption near-edge structure (XANES) spectroscopy of $MoS_2$@Fe-*N*-C NSs is situated between those of Fe foil and $Fe_2O_3$ references, elucidating that the oxidation state of isolate Fe atoms in $MoS_2$@Fe-*N*-C NSs is between 0 and +3 (26). More quantitative structural information of Fe can be readily documented by Fourier-transformed of extended X-ray absorption fine structure (FT-EXAFS) curves. As presented in Fig. 2*C*, $MoS_2$@Fe-*N*-C NSs shows a dominant peak at ~1.5 Å (without phase correction) ascribed to the Fe–N/O scattering path in the first shell (17), which is also seen in $Fe_2O_3$; in contrast, Fe foil reveals a dominant peak at 2.2 Å referring to the Fe-Fe scatting path. Moreover, only a small peak at ~2.2 Å is detected in $MoS_2$@Fe-*N*-C NSs, clearly indicating that a large proportion of Fe atoms are atomically dispersed and stabilized by nitrogen (27, 28). Furthermore, in $MoS_2$@Fe-*N*-C NSs, a clear satellite peak located on 3.05 Å, which could be categorized as a partial Fe atom

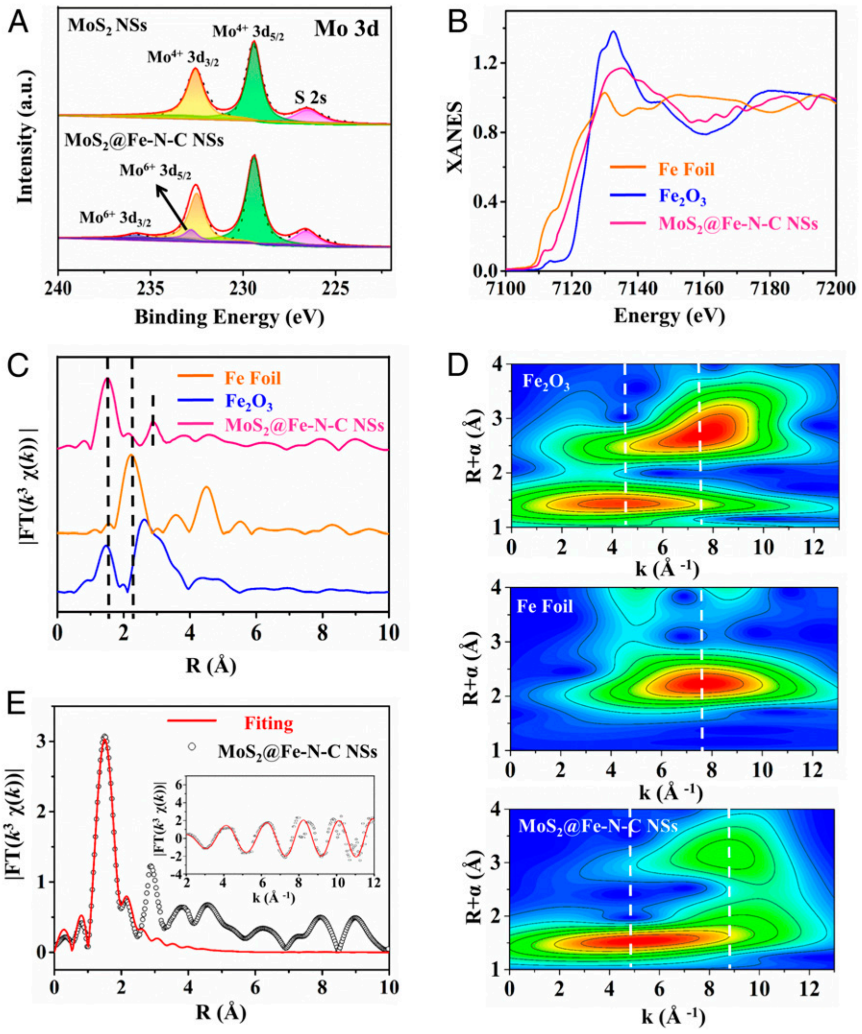

**Fig. 2.** (*A*) High-resolution Mo 3d XPS spectra. (*B*) Fe K-edge XANES spectra and (*C*) Fe K-edge k3-weighted FT spectra of single Fe atomic sites on MoS$_2$@Fe-*N*-C NSs, Fe$_2$O$_3$, and Fe foil samples, respectively. (*D*) WT of MoS$_2$@Fe-*N*-C NSs, Fe$_2$O$_3$, and Fe foil samples, respectively. (*E*) The corresponding EXAFS R space fitting curve; (*inset*) the corresponding EXAFS k space fitting curve of MoS$_2$@Fe-*N*-C NSs.

coordinated with a Mo atom in high-shell, owing to the strong electronic interactions at MoS$_2$/Fe-*N*-C interface (29). In addition, wavelet transform (WT) analysis was carried out, which provides a powerful resolution in k space and R space. Fig. 2*D* shows the WT analysis of MoS$_2$@Fe-*N*-C NSs with an intensity maximum emerged at ~4.3 Å$^{-1}$, assigned to the Fe-N coordination. In comparison, an intensity maximum at a higher k space of 7.6 Å$^{-1}$ occurs in Fe$_2$O$_3$, attributed to the Fe-Fe path (15). Notably, the weak peak intensity of MoS$_2$@Fe-*N*-C NSs at 8.9 Å$^{-1}$ indicates the existence of Fe-Mo coordination (30). According to the EXAFS fitting curve in Fig. 2*E* and fitting parameters in *SI Appendix*, Table S1, the best-fitting results clearly demonstrate that the first-shell peak at 1.5 Å can be ascribed to isolated Fe atoms coordinating with four N atoms as the Fe–N$_4$ structure, in comparison with the fitting results for Fe foil and Fe$_2$O$_3$ (*SI Appendix*, Fig. S9).

**Electrocatalytic Activities of MoS$_2$@Fe-*N*-C Nanospheres.** To evaluate the electrocatalytic performance of MoS$_2$@Fe-*N*-C NSs, MoS$_2$@Co-*N*-C NSs, and MoS$_2$@Ni-*N*-C NSs, the ORR were first investigated in a three-electrode cell using 0.1 M potassium hydroxide (KOH) solution saturated by oxygen. For comparison, the commercial Pt/C, Ir/C, and MoS$_2$ NSs (control sample) were tested as well. It should be noted that all the samples were directly attached to a glassy carbon electrode and then carefully studied on a rotating disk electrode. Specifically, the linear sweep voltammetry (LSV) curves demonstrate that MoS$_2$@Fe-*N*-C NSs possesses similar ORR half-wave potential ($E_{1/2}$) of 0.84 V (Fig. 3*A*) to Pt/C, more positive than those of MoS$_2$@Co-*N*-C NSs (0.80 V), MoS$_2$@Ni-*N*-C NSs (0.77 V), and MoS$_2$ NSs (0.76 V). More interestingly, the estimated Tafel slope of MoS$_2$@Fe-*N*-C NSs (84.7 mV·dec$^{-1}$) is even slightly lower than that of Pt/C (88.4 mV·dec$^{-1}$) (Fig. 3*B*), signifying its favorable ORR kinetics. Apart from the high activity, the MoS$_2$@Fe-*N*-C also exhibits a considerable ORR stability after 10,000 cycles ($\Delta E \approx 11$ mV, at a current density of 2.8 mA·cm$^{-2}$), which obviously outperforms that of Pt/C ($\Delta E \approx 34$ mV, at a current density of 2.8 mA·cm$^{-2}$) (*SI Appendix*, Fig. S10). To gain insight into the ORR mechanism, the ORR polarization curves were recorded at different rotation speeds, and the corresponding Koutecky–Levich (K–L) plots were obtained (*SI Appendix*, Fig. S11). All the K–L plots at different potentials show good linearity, indicating first-order reaction kinetics toward dissolved oxygen, and similar electron transfer number (*n*) during the ORR process. Based on the average values calculated from different potentials, the *n* of MoS$_2$@Fe-*N*-C NSs was calculated to be 3.82, close to the theoretical value of Pt/C (4.0) and much

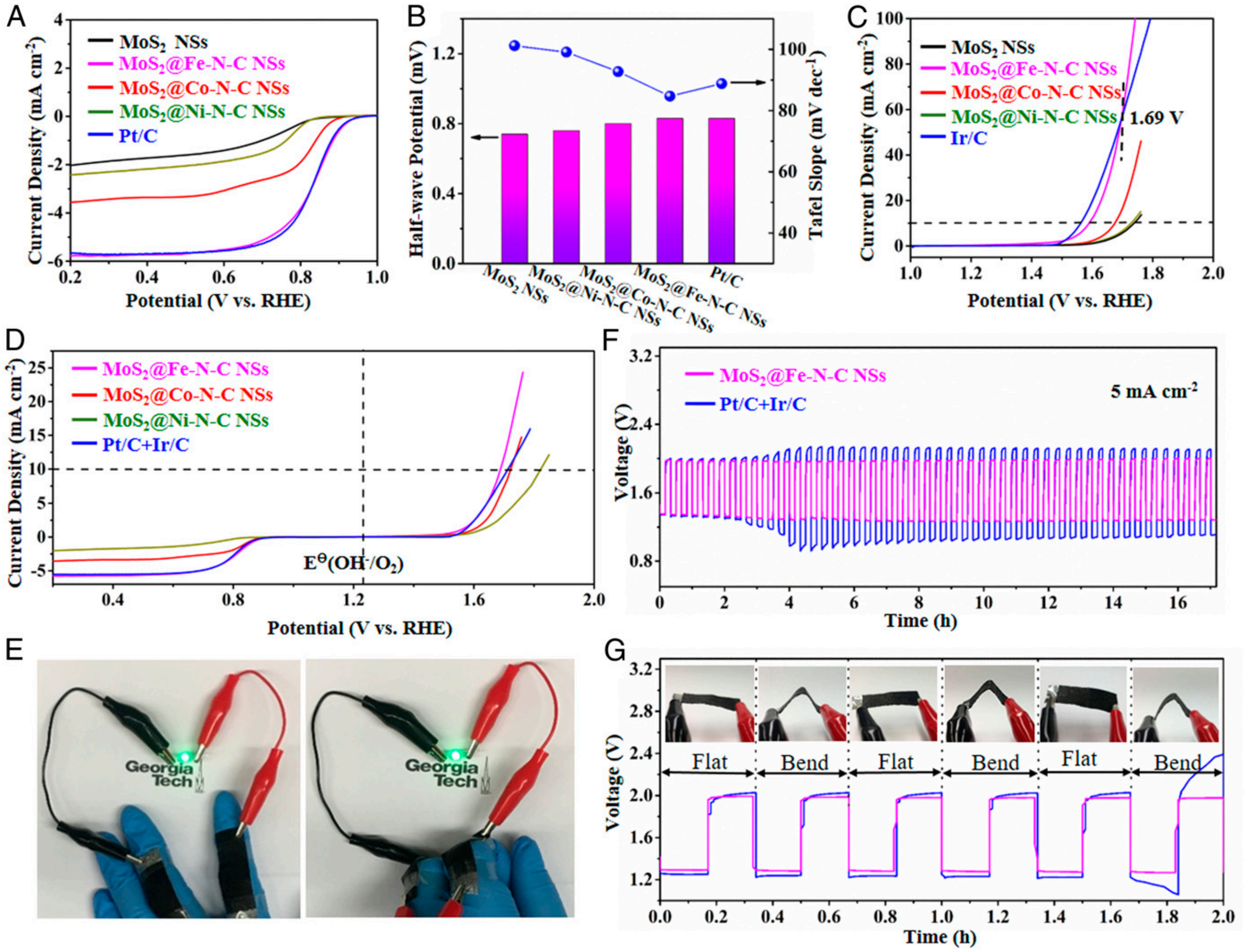

**Fig. 3.** (*A*) The ORR LSV curves of $MoS_2$@Fe-*N*-C NSs, $MoS_2$@Co-*N*-C NSs, $MoS_2$@Ni-*N*-C NSs, $MoS_2$ NSs, and Pt/C, respectively. (*B*) Comparison of half-wave potential (gradient-colored bars) and Tafel slope (blue circles). (*C*) The OER LSV curves of $MoS_2$@Fe-*N*-C NSs, $MoS_2$@Co-*N*-C NSs, $MoS_2$@Ni-*N*-C NSs, $MoS_2$ NSs, and Pt/C, respectively. (*D*) ORR/OER bifunctional LSV curves of $MoS_2$@Fe-*N*-C NSs, $MoS_2$@Co-*N*-C NSs, $MoS_2$@Ni-*N*-C NSs, $MoS_2$ NSs, and Pt/C+Ir/C, respectively. (*E*) Digital images of flat and bend wearable ZABs lighting a green LED. (*F*) The stability curves of the as-prepared wearable ZABs. (*G*) The charge–discharge curves of the wearable ZAB under repeated folding and releasing conditions.

larger than those of the $MoS_2$@Co-*N*-C NSs (3.62), $MoS_2$@Ni-*N*-C NSs (3.12), and $MoS_2$ NSs (3.05), suggesting that the $MoS_2$@Fe-*N*-C NSs manifest a better ORR performance. Taken together, these results clearly reveal that the $MoS_2$@Fe-*N*-C NSs, featuring multiple electrocatalytic activity sites (highly dispersed Fe atom, rich pyridinic N and graphitic N, and ample $MoS_2$/Fe-*N*-C interface), can function well in ORR because of improved oxygen adsorption (low onset potential), fast ion diffusion (high limiting diffusion current), and efficient electron transfer (electron transfer number ≈ 4).

It is intriguing to note that $MoS_2$@Fe-*N*-C NSs also reveals remarkable enhancement in OER performance in 1 M KOH (Fig. 3*C*), compared with $MoS_2$@Co-*N*-C NSs, $MoS_2$@Ni-*N*-C NSs (*SI Appendix*, Figs. S12 and S13, respectively), and $MoS_2$ NSs. Clearly, $MoS_2$@Fe-*N*-C NSs invokes a lower overpotential of 360 mV (at 10 $mA \cdot cm^{-2}$; close to that of Ir/C [330 mV]), contrasting sharply to those of $MoS_2$@Co-*N*-C NSs (440 mV), $MoS_2$@Ni-*N*-C NSs (500 mV), and $MoS_2$ NSs (510 mV). Interestingly, with a relatively low Tafel slope of 98.2 $mV \cdot dec^{-1}$ (*SI Appendix*, Fig. S14*A*), $MoS_2$@Fe-*N*-C NSs manifests the potential to exceed the current density of advanced Ir/C when the operating voltage is higher than 1.69 V (Fig. 3*C*). Most importantly, $MoS_2$@Fe-*N*-C NSs exhibits a superior OER stability ($\Delta E \approx 13$ mV) than Ir/C ($\Delta E \approx 27$ mV) after 10,000 cycles at 10 $mV \cdot cm^{-2}$ (*SI Appendix*, Fig. S14*B*). The outstanding OER performance of $MoS_2$@Fe-*N*-C NSs could be attributed to rich active sites on the grain boundary of the $MoS_2$ produced by radially arranged $MoS_2$ nanosheets and the coupling of $MoS_2$ and Fe-*N*-C at the MoS2/Fe-*N*-C interface.

The bifunctional catalytic activities of all samples were estimated by overall oxygen electrode activities, which is defined as the potential difference between OER and ORR (dented $\Delta E_{OEA} = E_{j\,=\,10} - E_{1/2}$, where $E_{j\,=\,10}$ represents the potential required to generate a current density of 10 $mA \cdot cm^{-2}$ for OER, and $E_{1/2}$ is the half-wave potential for ORR) in 0.1 M KOH (Fig. 3*D*). Notably, $MoS_2$@Fe-*N*-C NSs displays the lowest $\Delta E_{OEA}$ of 0.86 V, compared with $MoS_2$@Co-*N*-C NSs, $MoS_2$@Ni-*N*-C NSs, and Pt/C+Ir/C (a mixture of Pt/C and Ir/C at a 1:1 ratio) with $\Delta E_{OEA}$ values of 0.94 V, 1.06 V, and 0.90 V, respectively (*SI Appendix*, Fig. S15). Taken together, the superior activity of Fe single-atom sites and highly active $MoS_2$/Fe-*N*-C interface synergistically underpin outstanding bifunctional electrocatalytic performance, rendering $MoS_2$@Fe-*N*-C NSs as a promising candidate material for next-generation energy conversion and storage.

**Wearable ZAB Performances with $MoS_2$@Fe-*N*-C NSs Cathode.** In this context, $MoS_2$@Fe-*N*-C NSs were exploited as air cathode material for ZAB. Particularly, a flexible, thin-film solid-state ZAB was engineered, including a zinc foil, an alkaline polyvinyl alcohol gel solid-state electrolyte, and a catalyst-supported carbon cloth (*SI Appendix*, Fig. S16*A*), for wearable device applications. Due to its thinness (0.509 cm), the as-assembled all-solid-state ZAB can be bended or twisted considerably (*SI Appendix*, Fig. S16 *B–F*). The flexible ZAB with the $MoS_2$@Fe-*N*-C NSs cathode shows an open-circuit voltage of 1.47 V and a peak power density of 78 $mW \cdot cm^{-2}$, higher than that of Pt/C+Ir/C (1.43 V, 64 $mW \cdot cm^{-2}$; *SI Appendix*, Fig. S17*A*), respectively, consistent with its superior electrocatalytic ORR/OER activities as seen in the three-electrode system. Additionally, its special capacity can reach 442 $mAh \cdot g^{-1}{}_{Zn}$ at the current density of 5 $mA \cdot cm^{-2}$ (*SI Appendix*, Fig. S17b), corresponding to the energy density of 521 $Wh \cdot kg^{-1}$ (calculated by *SI Appendix*, Eq. S6). With the high-energy density characteristic, two flexible $MoS_2$@Fe-*N*-C NSs ZABs placed in series can light the light-emitting diode (LED), even bending by 180° (*SI Appendix*, Movie S1) or bending with the finger (Fig. 3*E*). Moreover, $MoS_2$@Fe-*N*-C NSs process excellent stability, representing no decrease in roundtrip efficiency (from 68.1 to 64.6%, only 3.5% decay) over 50 cycles at a constant current density of 5 $mA \cdot cm^{-2}$ (Fig. 3*F*). By contrast, the corresponding roundtrip efficiency of the Pt/C+Ir/C-based battery decreases from 68.1 to 46.7%. Importantly, the mechanical flexibility and stability tests of the $MoS_2$@Fe-*N*-C NSs-based battery was also performed by repeatedly bending and releasing the wearable battery for every charge–discharge cycle. As evidenced in Fig. 3*G*, the charge and discharge platforms of the $MoS_2$@Fe-*N*-C NSs-based battery display the smaller variations than that of the Pt/C+Ir/C-based reference battery, suggesting the excellent stability of $MoS_2$@Fe-*N*-C NSs in ZAB and the good rechargeability of the $MoS_2$@Fe-*N*-C NSs-based battery. Furthermore, ZAB with 6 M KOH as the electrolyte was also fabricated; the $MoS_2$@Fe-*N*-C NSs-based ZAB exhibits a high cycling stability when repeatedly charged and discharged for 22 h at a high current density of 10 $mA \cdot cm^{-2}$ at 2 h $cycle^{-1}$ rate without any significant drop of the overpotential (*SI Appendix*, Fig. S18*C*). In contrast, the severe polarization of the Pt/c+Ir/C-based ZAB occurs at the eighth cycle (i.e., 16 h), leading to the nonuniform distribution of current density at the electrode surface, and thus inevitably triggers the dendrite growth upon recharging (*SI Appendix*, Fig. S19) (31, 32).

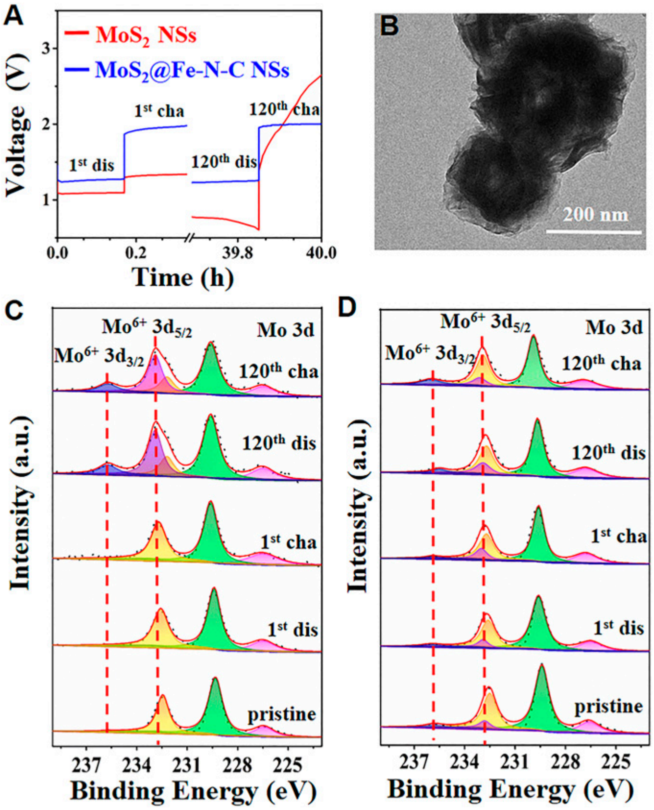

**Fig. 4.** (*A*) The galvanostatic discharge and charge voltage profile of $MoS_2$-based ZAB and $MoS_2$@Fe-*N*-C-based ZAB at 5.0 $mA \cdot cm^{-2}$ during the 1st and 120th cycles, respectively. TEM image of (*B*) $MoS_2$@Fe-*N*-C cathode after being cycled for 500 times. High-resolution XPS spectra of Mo 3d of (*C*) $MoS_2$ cathode and (*D*) $MoS_2$@Fe-*N*-C cathode obtained from the 1st discharge, 1st charge, 120th discharge, and 120th discharge processes.

**Interrogating the Long Cycling Stability Mechanism of $MoS_2$@Fe-*N*-C NSs.** To render a better understanding of the long-term cycling stability mechanism, it is essential to examine the component of the ZAB electrode during the cycling test. As control sample, $MoS_2$ NSs-based ZAB delivers a stable discharge and charge platform at 1.01 V and 1.32 V, respectively, during the first cycle (Fig. 4*A*). Notably, a sharp peak is emerged in the 120th cycle of the charging process in the $MoS_2$ NSs-based ZAB, indicating the severe polarization in the long-life cycles. In stark contrast, the $MoS_2$@Fe-*N*-C NSs-based ZAB possesses a similar and stable discharge and charge platform at 1.27 V and 2.01 V, respectively, during the first and 120th cycles, and manifests a 500-cycle (167 h) stability without visible polarization (*SI Appendix*, Fig. S20). To support the reversible long-life of the $MoS_2$@Fe-*N*-C NSs-based ZAB, we evaluated the morphology and structure of the ZAB electrode via TEM, XPS, X-ray diffraction (XRD), and Raman. As shown in Fig. 4*B* and *SI Appendix*, Fig. S21, partial $MoS_2$ NSs are broken into nanosheets after 120 cycles, while $MoS_2$@Fe-*N*-C NSs retain the spherical morphology after being cycled 500 times due to the protection of the Fe-*N*-C shell. To verify the oxidation of $MoS_2$ during the cycling test, XPS (Fig. 4 *C* and *D* and *SI Appendix*, Fig. S22), XRD (*SI Appendix*, Fig. S23), and Raman (*SI Appendix*, Fig. S24) measurements of the cathodes at various cycling stages were performed. High-resolution Mo 3d XPS spectra of the discharged $MoS_2$ NSs-based electrodes (120th cycle) exhibit two additional peaks at 232.7 eV and 235.7 eV, corresponding to $Mo^{6+}$ $3d_{5/2}$ and $Mo^{6+}$ $3d_{3/2}$, respectively, which could be ascribed to the oxidation of the partial $MoS_2$ (38.9%) during the long cycling. After the subsequent charging process, more $MoS_2$ is oxidized to $Mo^{6+}$, and the oxidized $Mo^{6+}$ species is estimated to be 45.1% (Fig. 4*C*). Likewise, almost 46.8% $S^{2-}$ in $MoS_2$ also are oxidized to $SO_4{}^{2-}$, after being cycled 120 times (*SI Appendix*, Fig. S22*A*). Moreover, the diffraction patterns of the $MoS_2$-based electrodes (first and 120th cycles) present three additional sharp peaks at 29.6°, 33.7°, and 39.6°, compared with that of the carbon paper substrate, corresponding to (1, 3, 0), (1, 1, 1) and (1, 5, 0) of $MoO_3$ (JCPDS card number 05-0508), respectively (*SI Appendix*, Fig. S23). Due to the high sensitivity of the Raman analysis, the surface chemical bond can be further studied by Raman (*SI Appendix*, Fig. S24). Two clear peaks at 821.4 and 992.3 $cm^{-1}$ manifest the formation of $MoO_3$ after the first cycle, which can be assigned to the doubly coordinated oxygen ($Mo_2$-O) stretching mode and the terminal oxygen (Mo = O) stretching mode (33, 34). Obviously, there are small $Mo^{6+}$ 3d peaks in high-resolution Mo 3d XPS spectra of the pristine $MoS_2$@Fe-*N*-C NSs, indicating the oxidation of slight $MoS_2$ (7.5%) due to carbonization of Fe-*N*-C shell (Fig. 4*D*). It is notable that only a small amount of $MoS_2$ is oxidized to $Mo^{6+}$ species (15.2%) and $SO_4{}^{2-}$ (14.7%) within 120 cycles (Fig. 4*D* and *SI Appendix*, Fig. S22*B*).

**Theoretical Modeling.** To further scrutinize the mechanism of high bifunctional reactivity and outstanding ORR/OER kinetics of $MoS_2$@Fe-*N*-C NSs over that of $MoS_2$ NSs, we conducted the first-principles-based density functional theory (DFT) calculations. It is well documented that the nonnoble metal center of single-atom active catalytic sites (M-$N_4$) experiences the high binding energy of oxygen and the low energy barrier for the four-electron ORR/OER pathway (35, 36). Thus, we built the theoretical models to understand the interfacial effect introduced by the Fe-*N*-C and $MoS_2$ layers. As depicted in *SI Appendix*, Fig. S25, the Fe-*N*-C layer is placed 3.06 Å away from the $MoS_2$ nanosheet, providing enough space for intermediates and products ($O_2$*, OOH*, O*, and OH*). As $O_2$* and OH* are the key intermediates from ORR and OER processes, we calculated electron density difference for $MoS_2$@Fe-*N*-C with these two adsorbed intermediates (Fig. 5 *A* and *B* and *SI Appendix*, Fig. S26). Clearly, the $MoS_2$ layer loses electrons (cyan in Fig. 5 *A* and *B*) and $O_2$* and OH* intermediates gains electrons (yellow in Fig. 5 *A* and *B*), suggesting that the $MoS_2$ layer is beneficial for electron transfer to adsorbed $O_2$ and OH on Fe-*N*-C, thereby promoting the generation of the OOH* intermediate (*SI Appendix*, Eq. S7). It is notable that N atoms in the Fe-*N*-C layer also transfer electrons to $O_2$* and OH* intermediates, demonstrating that the catalytically active sites are associated with the Fe centers coordinated to the nitrogen atoms (*SI Appendix*, Fig. S26). Moreover, Fig. 5*D* displays the calculated free energy pathways of the four-electron ORR reaction processes in alkaline condition. The free energy pathway is downhill at U = 0 V on $MoS_2$, $MoS_2$@Fe-*N*-C Sur (i.e., the Fe-*N*-C surface), and $MoS_2$@Fe-*N*-C Int (i.e., the $MoS_2$/Fe-*N*-C interface), revealing that all the electron transfer steps can occur spontaneously. The smallest negative free energy change (ΔG) from the first reaction step ($O_2+H_2O+e^- \rightarrow OOH^*+OH$; *SI Appendix*, Eq. S7) indicates the sluggish rate-determining step; and the energy barrier of $MoS_2$@Fe-*N*-C Int (−0.847 eV) is lower than that of $MoS_2$ (−0.173 eV) and $MoS_2$@Fe-*N*-C Sur (−0.905 eV) (Fig. 5*D*). Clearly, with the potential increased to 1.23 V (the energy levels for each net coupled proton and electron transfer step are shifted upward by 1.23 eV), the computed overpotential of $MoS_2$@Fe-*N*-C Int is 0.325 eV, which is also lower than that of $MoS_2$ (1.057 eV) and $MoS_2$@Fe-*N*-C Sur (0.383 eV) (Fig. 5*D*).

Furthermore, DFT calculations of free energy pathways of the OER processes on $MoS_2$, $MoS_2$@Fe-*N*-C Sur, and $MoS_2$@Fe-*N*-C Int suggest that the rate-limiting step lies in the third step ($O^*+OH+e^- \rightarrow OOH^*$), consistent with their energy barriers of 2.650, 2.199, and 1.857 eV, respectively (Fig. 5*E*). It is worth noting that $MoS_2$@Fe-*N*-C Int exhibits the lowest overpotential (0.627 eV) than that of $MoS_2$ (1.41 eV) and $MoS_2$@Fe-*N*-C Sur (0.889 eV). Taken together, the synergy of the $MoS_2$/Fe-*N*-C interface created by the interfacial charge transfer from Fe-*N*-C layer to the $MoS_2$ nanosheet and the single Fe active sites imparts low energy barriers, offering a theoretical foundation that accounts for superior bifunctional catalytic activity (ORR and OER) of $MoS_2$@Fe-*N*-C in alkaline medium.

## Conclusions

In summary, we developed a viable strategy to craft $MoS_2$@Fe-*N*-C NSs interfaced with single Fe atoms as a robust ORR/OER bifunctional electrocatalysts for wearable, high-capacity, and outstanding-cycling-stability ZABs. The $MoS_2$@Fe-*N*-C NSs accelerate sluggish ORR and OER kinetics and manifest excellent bifunctional catalytic performance in alkaline media. Moreover, DFT calculations reveal that the atomic dispersion of Fe coordinated by N atoms, in conjunction with the Fe-*N*-C shell draped over the $MoS_2$ core, contributes to the lower energy barriers of the intermediates, thereby resulting in high efficiency and active kinetics for ORR and OER. Furthermore, $MoS_2$@Fe-*N*-C NSs exhibit long-term cycling stability at a high current density for flexible, wearable ZABs, due largely to the suppression of oxidization of the $MoS_2$ core by the Fe-*N*-C shell. This work provides an effective paradigm to enhance catalytic kinetics and activity via interfacial engineering to introduce desired functionalities, which may be readily extended to design other high-efficiency catalysts.

## Materials and Methods

Additional details regarding the materials and methods may be found in the *SI Appendix*.

**Preparation of $MoS_2$@Fe-*N*-C Nanospheres ($MoS_2$@Fe-*N*-C NSs).** At first, 617 mg (0.5 mmol) ammonium molybdate ($(NH_4)_6Mo_7O_{24}{\cdot}4H_2O$), 533 mg (7 mmol)

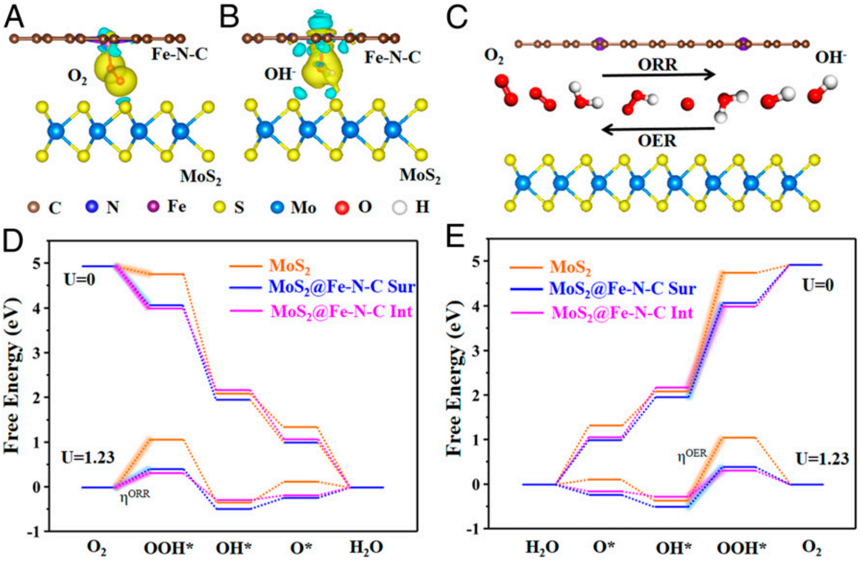

**Fig. 5.** Electron density difference plots for $MoS_2$@Fe-*N*-C with adsorbed (*A*) $O_2$ and (*B*) $OH^-$, respectively. The isosurface value of yellow and cyan regions are 0.003 $Bohr^{-3}$. Yellow contours represent charge accumulations, and cyan contours denote charge depletion. (*C*) Schematic of $O_2$ intercalation at the $MoS_2$/Fe-*N*-C interface, and the production of $OH^-$ during the ORR process as well as its reverse process (OER process). Free energy diagrams of (*D*) ORR and (*E*) OER on $MoS_2$, $MoS_2$@Fe-*N*-C surface, and $MoS_2$@Fe-*N*-C interface at U = 0 V and U = 1.23 V, respectively.

thiourea ($NH_2CSNH_2$,), and 300 mg (0.005 mmol) surfactant PVP were dissolved in 17 mL of deionized water under vigorous stirring to form a homogeneous solution. Then, the solution was transferred into a 50 mL Teflon-lined stainless steel autoclave and kept at 220 °C for 18 h. After being cooled to room temperature, the generated precipitates ($MoS_2$ nanospheres) were centrifuged and washed with water and ethanol several times. The $MoS_2$ nanospheres coated with PDA (denoted $MoS_2$@PDA) were synthesized by polymerization of dopamine in Tris buffer (pH 8.5). Then, 250 mg DICY was dispersed into 10 mL deionized water containing 50 mg $FeCl_3$, forming a uniform solution. A total of 100 mg of $MoS_2$@PDA was then introduced into the above solution and stirred for 3 h. Afterwards, the obtained suspension was vacuum-dried at 50 °C, followed by heat treatment at 800 °C for 2 h under $N_2$ atmosphere.

**Data Availability.** All study data are included in the article and/or supporting information.

**ACKNOWLEDGMENTS.** We are grateful for financial support from the Priority Academic Program Development of Jiangsu Higher Education Institutions. Y.Y. acknowledges financial support from Jiangsu Normal University.

1. X. Han *et al*., Metal-air batteries: From static to flow system. *Adv. Energy Mater.* **8**, 1801396 (2018).
2. Y. Li, H. Dai, Recent advances in zinc-air batteries. *Chem. Soc. Rev.* **43**, 5257–5275 (2014).
3. J. Zhang, Q. Zhou, Y. Tang, L. Zhang, Y. Li, Zinc-air batteries: Are they ready for prime time? *Chem. Sci. (Camb.)* **10**, 8924–8929 (2019).
4. P. Tan *et al*., Flexible Zn– and Li–air batteries: Recent advances, challenges, and future perspectives. *Energy Environ. Sci.* **10**, 2056–2080 (2017).
5. P. Prabhu, V. Jose, J.-M. Lee, Design strategies for development of TMD-based heterostructures in electrochemical energy systems. *Matter* **2**, 526–553 (2020).
6. M. Liu *et al*., Conductive carbon nanofiber interpenetrated graphene architecture for ultra-stable sodium ion battery. *Nat. Commun.* **10**, 3917 (2019).
7. J. Zhu *et al*., Boundary activated hydrogen evolution reaction on monolayer $MoS_2$. *Nat. Commun.* **10**, 1348 (2019).
8. Y. Yang, H. Fei, G. Ruan, C. Xiang, J. M. Tour, Edge-oriented $MoS_2$ nanoporous films as flexible electrodes for hydrogen evolution reactions and supercapacitor devices. *Adv. Mater.* **26**, 8163–8168 (2014).
9. H. Li *et al*., Corrigendum: Activating and optimizing $MoS_2$ basal planes for hydrogen evolution through the formation of strained sulphur vacancies. *Nat. Mater.* **15**, 364 (2016).
10. X. J. Chua *et al*., Negative electrocatalytic effects of p-doping niobium and tantalum on $MoS_2$ and $WS_2$ for the hydrogen evolution reaction and oxygen reduction reaction. *ACS Catal.* **6**, 5724–5734 (2016).
11. J. Zhang *et al*., Interface engineering of $MoS_2$/$Ni_3$ $S_2$ heterostructures for highly enhanced electrochemical overall-water-splitting activity. *Angew. Chem. Int. Ed. Engl.* **55**, 6702–6707 (2016).
12. I. S. Amiinu *et al*., Multifunctional Mo-N/C@$MoS_2$ electrocatalysts for HER, OER, ORR, and Zn-Air batteries. *Adv. Funct. Mater.* **27**, 1702300 (2017).
13. B. Mohanty *et al*., $MoS_2$ quantum dots as efficient catalyst materials for the oxygen evolution reaction. *ACS Catal.* **8**, 1683–1689 (2018).
14. L. Jiao *et al*., When nanozymes meet single-atom catalysis. *Angew. Chem. Int. Ed. Engl.* **59**, 2565–2576 (2020).
15. Y. Chen *et al*., Enhanced oxygen reduction with single-atomic-site iron catalysts for a zinc-air battery and hydrogen-air fuel cell. *Nat. Commun.* **9**, 5422 (2018).
16. C. Zhu, S. Fu, Q. Shi, D. Du, Y. Lin, Single-atom electrocatalysts. *Angew. Chem. Int. Ed. Engl.* **56**, 13944–13960 (2017).
17. Y. Chen *et al*., Atomic Fe dispersed on N-doped carbon hollow nanospheres for high-efficiency electrocatalytic oxygen reduction. *Adv. Mater.* **31**, e1806312 (2019).
18. A. Bakandritsos *et al*., Mixed-valence single-atom catalyst derived from functionalized Graphene. *Adv. Mater.* **31**, e1900323 (2019).
19. S. Zhang, B. V. R. Chowdari, Z. Wen, J. Jin, J. Yang, Constructing highly oriented configuration by few-layer $MoS_2$: Toward high-performance lithium-ion batteries and hydrogen evolution reactions. *ACS Nano* **9**, 12464–12472 (2015).
20. Y. Wang *et al*., Visible-light driven overall conversion of $CO_2$ and $H_2O$ to $CH_4$ and $O_2$ on 3D-SiC@2D-$MoS_2$ heterostructure. *J. Am. Chem. Soc.* **140**, 14595–14598 (2018).
21. S. Rathi *et al*., Tunable electrical and optical characteristics in monolayer graphene and few-layer $MoS_2$ heterostructure devices. *Nano Lett.* **15**, 5017–5024 (2015).
22. P. Chen *et al*., Nitrogen-doped nanoporous carbon nanosheets derived from plant biomass: An efficient catalyst for oxygen reduction reaction. *Energy Environ. Sci.* **7**, 4095–4103 (2014).
23. M. Zhang *et al*., Metal (Hydr)oxides@polymer core-shell strategy to metal single-atom materials. *J. Am. Chem. Soc.* **139**, 10976–10979 (2017).
24. M. Xiao *et al*., Microporous framework induced synthesis of single-atom dispersed Fe-N-C acidic ORR catalyst and its in situ reduced Fe-$N_4$ active site identification revealed by X-ray absorption spectroscopy. *ACS Catal.* **8**, 2824–2832 (2018).
25. L. Lin, Q. Zhu, A.-W. Xu, Noble-metal-free Fe-N/C catalyst for highly efficient oxygen reduction reaction under both alkaline and acidic conditions. *J. Am. Chem. Soc.* **136**, 11027–11033 (2014).
26. Z. Yang *et al*., Boosting oxygen reduction catalysis with Fe–$N_4$ sites decorated porous carbons toward fuel cells. *ACS Catal.* **9**, 2158–2163 (2019).
27. Q. Liu, X. Liu, L. Zheng, J. Shui, The solid-phase synthesis of an Fe-N-C electrocatalyst for high-power proton-exchange membrane fuel cells. *Angew. Chem. Int. Ed. Engl.* **57**, 1204–1208 (2018).
28. J. Wang *et al*., Synergistic effect of well-defined dual sites boosting the oxygen reduction reaction. *Energy Environ. Sci.* **11**, 3375–3379 (2018).
29. W. Qu *et al*., Single-atom catalysts reveal the dinuclear characteristic of active sites in NO selective reduction with $NH_3$. *Nat. Commun.* **11**, 1532 (2020).
30. Y. K. Li, G. Zhang, W. T. Lu, F. F. Cao, Amorphous Ni-Fe-Mo suboxides coupled with Ni network as porous nanoplate array on nickel foam: A highly efficient and durable bifunctional electrode for overall water splitting. *Adv. Sci. (Weinh.)* **7**, 1902034 (2020).
31. K. Wang *et al*., Dendrite growth in the recharging process of zinc–air batteries. *J. Mater. Chem. A Mater. Energy Sustain.* **3**, 22648–22655 (2015).
32. J. Yi *et al*., Challenges, mitigation strategies and perspectives in development of zinc-electrode materials and fabrication for rechargeable zinc–air batteries. *Energy Environ. Sci.* **11**, 3075–3095 (2018).
33. M. Ledendecker, G. Clavel, M. Antonietti, M. Shalom, Highly porous materials as tunable electrocatalysts for the hydrogen and oxygen evolution reaction. *Adv. Funct. Mater.* **25**, 393–399 (2015).
34. K. Yan, Y. Lu, Direct growth of $MoS_2$ microspheres on Ni foam as a hybrid nanocomposite efficient for oxygen evolution reaction. *Small* **12**, 2975–2981 (2016).
35. S. Kattel, G. Wang, A density functional theory study of oxygen reduction reaction on Me–$N_4$ (Me = Fe, Co, or Ni) clusters between graphitic pores. *J. Mater. Chem. A Mater. Energy Sustain.* **1**, 10790–10797 (2013).
36. J. Zhang *et al*., Tuning the coordination environment in single-atom catalysts to achieve highly efficient oxygen reduction reactions. *J. Am. Chem. Soc.* **141**, 20118–20126 (2019).